Summer 7-6-2022

Deformation of Antigorite + Olivine Aggregates: Implications for Mantle Wedge Dynamics

Roselyn K. Hurlow

Roselyn Hurlow
Candidate

Earth and Planetary Sciences
Department

This thesis is approved, and it is acceptable in quality and form for publication:

Approved by the Thesis Committee:

Dr. Jin Zhang , Chairperson

Dr. Lowell Miyagi

Dr. Brandon Schmandt

DEFORMATION OF ANTIGORITE + OLIVINE AGGREAGTES: IMPLICATIONS FOR MANTLE WEDGE DYNAMICS

by

ROSELYN HURLOW

B.S. GEOLOGY,
UNIVERSITY OF UTAH

THESIS

Submitted in Partial Fulfillment of the
Requirements for the Degree of

Master of Science
Earth and Planetary Sciences

The University of New Mexico,
Albuquerque, New Mexico,

July 2022

Deformation of Antigorite + Olivine Aggregates: Implications for Mantle Wedge Dynamics

by

Roselyn Hurlow

B.S., Geology, University of Utah, 2019

M.S., Earth and Planetary Sciences, University of New Mexico, 2022

ABSTRACT

Aggregates with varying volume proportions of antigorite and olivine were deformed at mantle wedge conditions of high-pressure (P) (2.5-7.6 GPa), -temperature (T) (675 K), and strain rates from ~$1.0*10^{-5}$ to ~$1.0*10^{-4}$ s^{-1} using the deformation-DIA (D-DIA) to investigate deformation mechanisms and stress/strain partitioning. Macroscopic strain, lattice strain, and texture were measured in situ using synchrotron x-ray diffraction and radiography and were modeled for olivine using Elasto-Viscoplastic Self-Consistent (EVPSC) simulations. These modeled results are coupled with microstructure images and electron backscatter diffraction (EBSD) measurements results to determine stress and deformation mechanisms. Previous to this study, investigations have been limited to static microscopy studies of exhumed serpentinized peridotites or single-phase deformation experiments. Our results demonstrate the importance and feasibility of evaluating complicated geologic settings like the mantle wedge with more accurate multiphase systems for in situ observations. Antigorite, the softer mineral, is the strain-accommodating phase, and deforms like a single phase when mixed with olivine, the harder mineral. When the vol.% of olivine increases, most of the stress seems to be accepted into the strong

framework, increasing aggregate stress. This observation could have implications for determining the maximum depth of decoupling, which is dependent on the strength contrast between the serpentinized interface layer above a subducting slab and the mantle wedge. Olivine's deformation is primarily through activity of unidirectional kink systems with influence from pencil glide ang B-type slip. We see a change in dominant slip systems when the starting sample was polished so the initial aggregate texture was rotated, implying the orientation of antigorite and/or olivine effects transient deformation of these aggregates. We conclude the distribution of stress, strain, and anisotropy in the forearc mantle wedge will vary with the degree of serpentinization, which in turn varies with depth and other local subduction zone attributes such as temperature and rate of subduction.

TABLE OF CONTENTS

LIST OF FIGURES

LIST OF TABLES

1. INTRODUCTION

The mantle wedge is the unique section of the uppermost mantle above a subducting slab and below the lithosphere of the overriding plate, stretching from the forearc through the volcanic arc. This dynamic area defines some of the most complicated, and occasionally hazardous, earth processes like arc magmatism, volatile circulation, and mantle flow. Rheological properties and deformation mechanisms of mantle wedge materials are key parameters in geodynamic and geophysical interpretations of this region, such as wedge flow models and trench-parallel seismic anisotropy patterns [e.g. Kamiya and Kobayashi, 2000, van Keken et al., 2002, Long and van der Hilst, 2006, Wada et al., 2008, Wiens et al., 2008, Long and Wirth, 2013, Kenyon and Wada, 2022]. These investigations acknowledge the contribution from olivine and/or antigorite textures and viscosities to the observed anisotropy and dynamics. Specifically, the orientation of antigorite's basal plane parallel to the subducting slab surface and B-type olivine fabrics are of particular importance due to the large water flux from slab dehydration and strain induced by subduction of slabs. Both high-P and -T deformation experiments [Zhang and Karato, 1995, Hilairet et al., 2007 & 2012, Katayama et al., 2004 & 2009, Katayama and Karato, 2008, Burnley, 2015, Burnley and Kaboli, 2019] and ex-situ studies of natural exhumed serpentinized peridotites [Nishii et al., 2011, Soda and Wenk, 2013, Auzende et al., 2015, Morales et al., 2018, Horn et al., 2020] provide constraints to flow behaviors and textures of antigorite and olivine in the mantle wedge.

Although the ex-situ studies of rocks containing both antigorite and olivine provide fair documentation of their textural relationships, the in-situ experiments have been restricted to deformation of just one phase. Even if we have a good understanding of how

a single phase deforms, deformation behavior of two or more phases cannot typically be predicted. Handy (1990, 1994) defines two basic multiphase structures based on their viscous strength contrast: a load-bearing framework (LBF) and interconnected layers of the weak phase (IWL). When the strong phase is interconnected, as in the LBF structure, most of the stress is accepted by the framework, increasing aggregate yield strength. When the weak phase is interconnected and the strong phase forms boudin-like structures, as in the IWL structure, most of the strain is partitioned to the weak phase, decreasing aggregate yield strength. Recent studies of multiphase deformation experiments conducted on lower-mantle materials highlight strain and stress partitioning in aggregates due to varying proportions of intrinsically hard and soft phases, microstructures, and phase interactions [e.g. Kaercher et al., 2016, Miyagi and Wenk, 2016, Girard et al., 2016, Lin et al., 2019, Chandler et al., 2021]. Furthermore, texture development and intensity can be altered by multiphase interactions changing plastic deformation mechanisms through strain accommodation of the weak phase [Wang et al., 2013, Lin et al., 2019, Kasemer et al., 2020].

Hilairet et al., (2007) documents the substantial viscous strength contrast between antigorite and olivine under mantle wedge pressures, temperatures, and strain rates. This implies that if these phases were deformed together, as they likely are in the mantle wedge, increasing volume percentage of antigorite (the weak phase) to olivine (the strong phase) may decrease overall strength and change olivine's texture development within the mantle wedge. Although mantle wedge assemblies typically include more minerals that just olivine and serpentine (Grove et al., 2012), the deformation study of an antigorite + olivine two phase mixture will still shed light on the overall deformation behaviors of the strong

(e.g. olivine, pyroxenes etc.) and weak (e.g. antigorite, chlorite etc.) phases existent in the region. Thus, we studied textures and lattice strain evolution in olivine + antigorite aggregates of varying volume percentages deformed using the D-DIA under mantle wedge conditions up to ~7 GPa, 400 C, and 25% macroscopic strain. We compare our experimental results with EVPSC simulations and EBSD to obtain information about stress-strain partitioning, texture development, and aggregate strengths.

2. EXPERIMENTS

Natural samples of San-Carlos olivine and antigorite from Estancia de La Virgen in the Motagua Mélange in Guatemala (American Museum of Natural History, sample specimen MVJ87-6-2) were separately ground to a grain size varying from ~5-50 µm. These samples were then mixed in varying phase volume proportions and sintered at 3 GPa and 400 K for 3 hrs using the 2000-ton Multi Anvil Press at the High-Pressure Lab at University of New Mexico (UNM), NM. The resultant "rock" cylinders of ~4.5 mm in length and 1.6 mm in diameter were then cut in half and polished to 1.2 mm in length and 1.2 mm in diameter for deformation experiments. All but one sample were polished so antigorite's basal planes were oriented perpendicular to the axial compression direction of the D-DIA. The final sample, deformed in experiment D2708, was polished so the antigorite basal planes were oriented at ~45° to the axial compression direction to investigate the dependency of deformation on pre-existing textures (Figure 1).

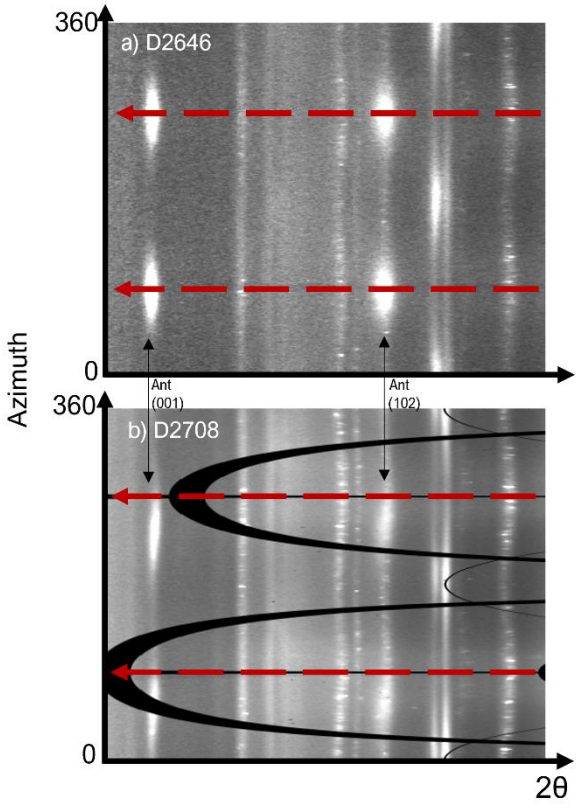

Figure 1. Unrolled diffraction images of (a) experiment D2646 and (b) experiment D2708 at ~2% macroscopic strain. Red dashed lines show compression direction, correlating to ~90° and 270° azimuth and demonstrate the angle of antigorite basal planes (shown with Ant(001) and Ant(102)). in (a), the basal planes are perpendicular to compression direction. In (b), the basal planes are rotated ~40° to compression direction.

Deformation experiments were performed using the D-DIA located at beamline 13-BM-D at the Advanced Photon Source, Argonne National

Laboratory, IL. The polished cylinders were loaded in a cubic cell assembly (Figure 2) suited for 4 mm truncation anvils. Table 1 summarizes all the experiments. The D-DIA allows for control of differential stress through the independent advancement of the top and bottom anvils at the desired temperature and hydrostatic pressure, shortening the sample. X-ray radiographs were collected *in-situ* to determine axial strain through:

$$\varepsilon = (l - l_0)/l_0, \quad (1)$$

where l is the sample length during the deformation experiments and l_0 is the initial sample length, which are defined by Ni or Au foil placed on the top and bottom of the sample. Radiographs were acquired over 10 s using a YAG scintillator and a charged coupled device (CCD). This radiograph collection alternated with 2-dimensional x-ray diffraction (XRD) image collection over 400 to 600 s. The synchrotron X-ray beam entered the sample through a gap between the anvils which allowed for ~10° opening angle in 2θ. The detectors used (MARCCD, Pilatus) allowed for a full 360° coverage, and images were calibrated using an Al_2O_3 standard. Detector distances and X-ray wavelengths varied for each experiment (Table 1).

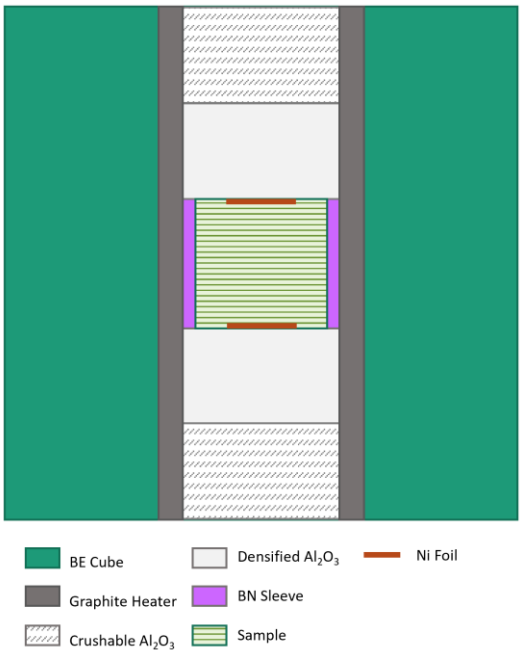

Figure 2. Sample assembly for D-DIA experiments. The foil is either Ni or Au with a thickness of ~0.1 µm (not to scale). The stripes in the sample schematically represent the orientation of antigorite's basal cleavage for all experiments except D2708.

The deformed samples were recovered and polished into thin sections for post-experiment microstructural, grain size, and textural analyses. The microstructure was analyzed using the scanning electron microscope (SEM)

at the Earth and Planetary Sciences department at UNM. EBSD analysis was conducted on the thin sections at the State Key Laboratory for Mineral Deposits Research in Nanjing University, Nanjing, China.

Table 1. Experimental Conditions

Run Number	Antigorite/Olivine Volume Ratio	Refined Detector Distance (nm)	Wavelength (Å)	P[a] (GPa)	Strain Rate ($*10^{-5}$ s^{-1})		Maximum Strain (%)
					[b]	[c]	
D2608	70/30	464.08	0.225	6.77	0.44	8.52	23.1
D2609	70/30	464.36	0.225	2.56	1.36	11.80	23.1
D2646	50/50	465.67	0.225	7.09	1.42	10.20	22.6
D2647	50/50	465.67	0.225	3.78	1.09	7.80	20.4
D2703	20/80	493.55	0.264	3.54	1.06	8.16	20.4
D2705	20/80	492.98	0.264	6.44	1.06	8.91	21.6
D2708[d]	50/50	495.68	0.264	7.67	1.23	7.96	20.8

[a]At last data point, from olivine
[b]During initial differential ram speed
[c]During secondary differential ram speed
[d]Sample was rotated ~45°

3. EXPERIMENT DATA ANALYSIS

3.1. Lattice Strains and Stress

The D-DIA has an axial compression direction, which allows the stress state at the center of the sample to be broken down to a hydrostatic and deviatoric component given by

$$\sigma_{ij} = \begin{bmatrix} \sigma_{11} & 0 & 0 \\ 0 & \sigma_{22} & 0 \\ 0 & 0 & \sigma_{33} \end{bmatrix}$$

$$= \begin{bmatrix} \sigma_P & 0 & 0 \\ 0 & \sigma_P & 0 \\ 0 & 0 & \sigma_P \end{bmatrix} + \begin{bmatrix} -t/3 & 0 & 0 \\ 0 & -t/3 & 0 \\ 0 & 0 & 2t/3 \end{bmatrix}, \quad (2)$$

where σ_P is the hydrostatic stress and t is the uniaxial stress component ($\sigma_{33} - \sigma_{11}$). When a deviatoric stress is applied to the material, the measured d-spacings, $d_m(hkl)$, are a function of the angle, ψ, between the diffraction vector and the compression direction. The relationship between $d_m(hkl)$ and the lattice stain, $Q(hkl)$ or "Q-factor", is [Singh et al., 1998]

$$d_m(hkl) = d_p(hkl)[1 + (1 - 3cos^2\psi)Q(hkl)], \quad (3)$$

where $d_p(hkl)$ is the d-spacing solely under σ_P. When the sample is under hydrostatic stress, $Q(hkl)$ is 0, but as deviatoric stress increases, d_m shifts from d_p for a plane (hkl), and lattice strain increases (Figure 3).

Confining pressures for both phases were determined using unit cell volumes calculated from d_p and a third order Birch-Murnaghan equation of state [Birch, 1947]

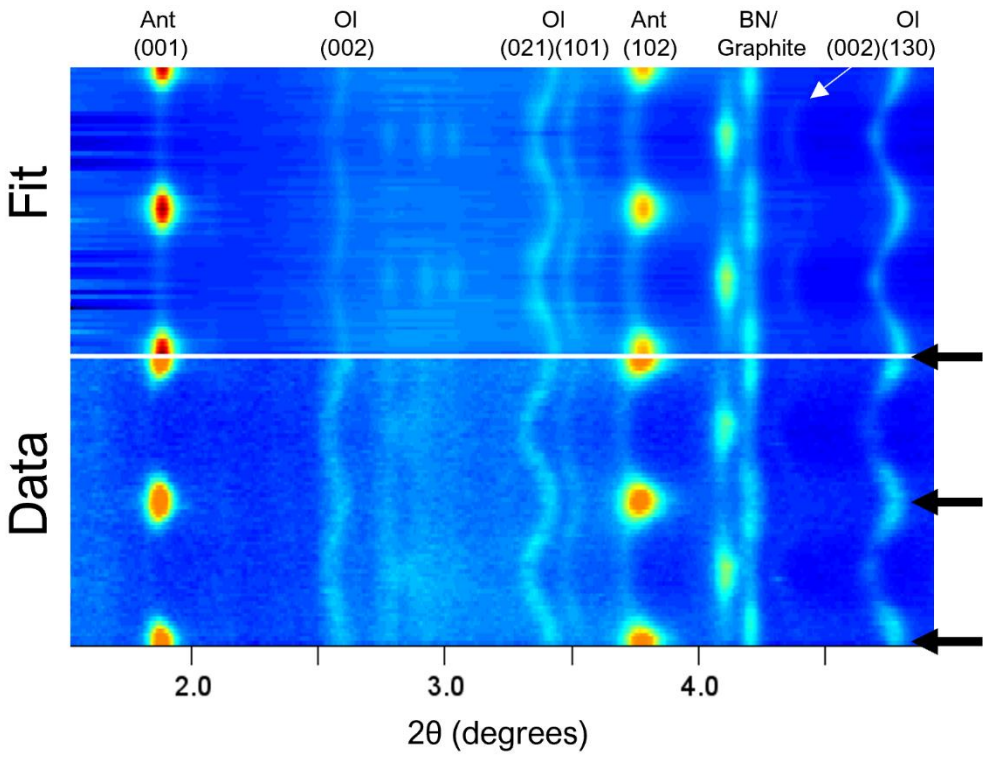

Figure 3. An unrolled diffraction image and MAUD fit of experiment D2647 at ~11% strain. Systematic intensity variations along azimuth indicate texture and sinusoidal variations indicate lattice strain.

$$P(V) = \frac{3}{2}K_0\left[\left(\frac{V_0}{V}\right)^{\frac{7}{3}} - \left(\frac{V_0}{V}\right)^{\frac{5}{3}}\right] \times \left\{1 + \frac{3}{4}(K_0' - 4)\left[\left(\frac{V_0}{V}\right)^{\frac{2}{3}} - 1\right]\right\}, \quad (4)$$

where V is the measured unit cell volume and V_0, K_0, and K_0' are the unit cell volume, bulk modulus, and pressure derivative of the bulk modulus at room pressure, respectively. To determine the pressure in olivine, we used the EOS parameters derived by Zhang and Bass (2016), and to determine the pressure in antigorite, we used the EOS parameters derived by Bezacier et al., (2013).

To estimate differential stress, t, we used the empirical equation [Singh et al., 1998]

$$t(hkl) = 6GQ(hkl), \quad (5)$$

where G is the shear modulus. G was calculated at the desired P at T for olivine and antigorite using the single crystal elastic properties from by Zhang and Bass (2016) and Bezacier et al., (2013), respectively. However, this estimation of t is biased based on the availability of diffraction lines and has no physical grounding [e.g., Li et al., 2004, Burnley and Zhang, 2008]. Olivine's flow stress expressed later with the EVPSC modeling is a more appropriate approximation.

3.2. Textures

Synchrotron X-ray diffraction images were analyzed using the software MAUD [Lutterotti et al., 1997]. Refinements generally followed the procedure for analysis of polymineralic shale outlined in Wenk et al. (2014). The texture of antigorite and olivine was refined using the E-WIMV algorithm which is a modification of the WIMV method [Matthies and Vinel, 1982] (Figure 3). Fiber symmetry was imposed on the Orientation Distribution Function (ODF) for both phases, which was then exported from MAUD and smoothed using an 7.5° Gauss filter in the program BEARTEX [Wenk et al., 1998]. Textures are expressed with Inverse Pole Figures (IPF), which show the density of crystallographic axes relative to the compression direction ([001]) in multiples of random distribution (m.r.d.), where a value of 1 corresponds to a completely random distribution of axes. In the case of a perfectly oriented sample (say, a single crystal) the m.r.d. would be equal to infinity for one orientation, and 0 for all others.

When conducting textural analyses, the crystallographic parameters of monoclinic minerals such as antigorite can be expressed in two settings; the first has the C_2 rotation axis parallel to the z axis, and the second, which is more geologically traditional, has the C_2 rotation axis parallel to the y axis [Matthies and Wenk, 2009]. Here, we use the first

setting, as it is necessary for the analytical software used in this study. Until the discussion section of this study, the basal plane of antigorite will be referred to as the (100) plane, instead of the more common (001) notation.

3.3. EVPSC Modeling

EVPSC modeling [Wang et al., 2010] is an effective medium self-consistent method utilized for linking the activity of slip systems to observed lattice strains, producing model textures, and as stated previously, evaluating macroscopic stress. Like other self-consistent methods (e.g., Visco-Plastic Self-Consistent (VPSC) code [Lebensohn and Tomé, 1994] and Elasto-Plastic Self-Consistent (EPSC) code [Turner and Tomé, 1994]), the EVPSC model treats each grain as an inclusion in a homogenous anisotropic matrix that has the averaged properties of the polycrystal [Wang et al., 2010], but allows a continuous elasto-plastic transition. As deformation proceeds in the model, the inclusion and matrix interact and the macroscopic elasto-plastic properties are iteratively updated until the average strain and stress match the macroscopic strain and stress.

In the EVPSC code, the rate-sensitive constitutive law that defines the plastic behavior of the inclusions is

$$\dot{\varepsilon}_{ij} = \dot{\gamma}_0 \sum\nolimits_s m_{ij}^s \left\{\frac{m_{kl}^s \sigma_{kl}}{\tau^s}\right\}^n, \tag{6}$$

where $\dot{\varepsilon}_{ij}$ is the strain rate, $\dot{\gamma}_0$ is the reference shear strain rate, m_{kl}^s is the symmetric Schmid factor for the slip system, s, σ_{kl} is the local stress tensor, τ^s is the rate sensitive critical resolved shear stress (CRSS) of a slip system, and n is the stress exponent. The code bases which deformation mode is active on the CRSS value and increments the stress

into each iterative grain accordingly. The evolution of each plastic mechanism on the slip planes is expressed using an empirical Voce hardening law [Tomé et al., 1984]

$$\tau^s = \tau_0^s + (\tau_1^s + \theta_1^s \Gamma) \cdot \left(1 - \exp\left[-\frac{\theta_0^s \Gamma}{\tau_1^s}\right]\right), \quad (7)$$

where Γ is the accumulated shear in the grain, τ_0^s is the initial CRSS, and θ_0^s and θ_1^s are the initial and asymptotic hardening rates, respectively.

Although multi-phase modeling is one of the benefits of using the EVPSC code, we only show modeled results for olivine. In this study, only the (100) and (210) lattice reflections were processable for antigorite, leaving us with an incomplete picture of the strained unit cell, making EVPSC not useful for evaluating the mechanical properties of monoclinic antigorite. In contrast, olivine has an abundance of strong lattice reflections, allowing for a successful match of Q-factors with slip systems using EVPSC.

Because we are modeling one phase in a two-phase experiment and assuming there is uneven strain partitioning, the strain rate used for EVPSC should not be the same as the macroscopic values shown in Table 1. To produce a strain rate more appropriate for solely modeling olivine in EVPSC, we evaluated strain partitioning between the two phases. SEM images were used to estimate relative aspect ratio changes from pre- to post-deformation grains (Figure 4). Olivine's (021), (101), (002), and (130) reflections were selected for modeling. The parameters used for EVPSC modeling are listed in Table 2. Similar to the methods described in Burnley et al., (2015), we used seven commonly observed slip systems in olivine and included three unidirectional slip systems representative of kink bands. Our best stress fit was achieved with the tangent homogenization scheme which allows a more heterogenous strain from grain to grain and tends to predict a uniform stress

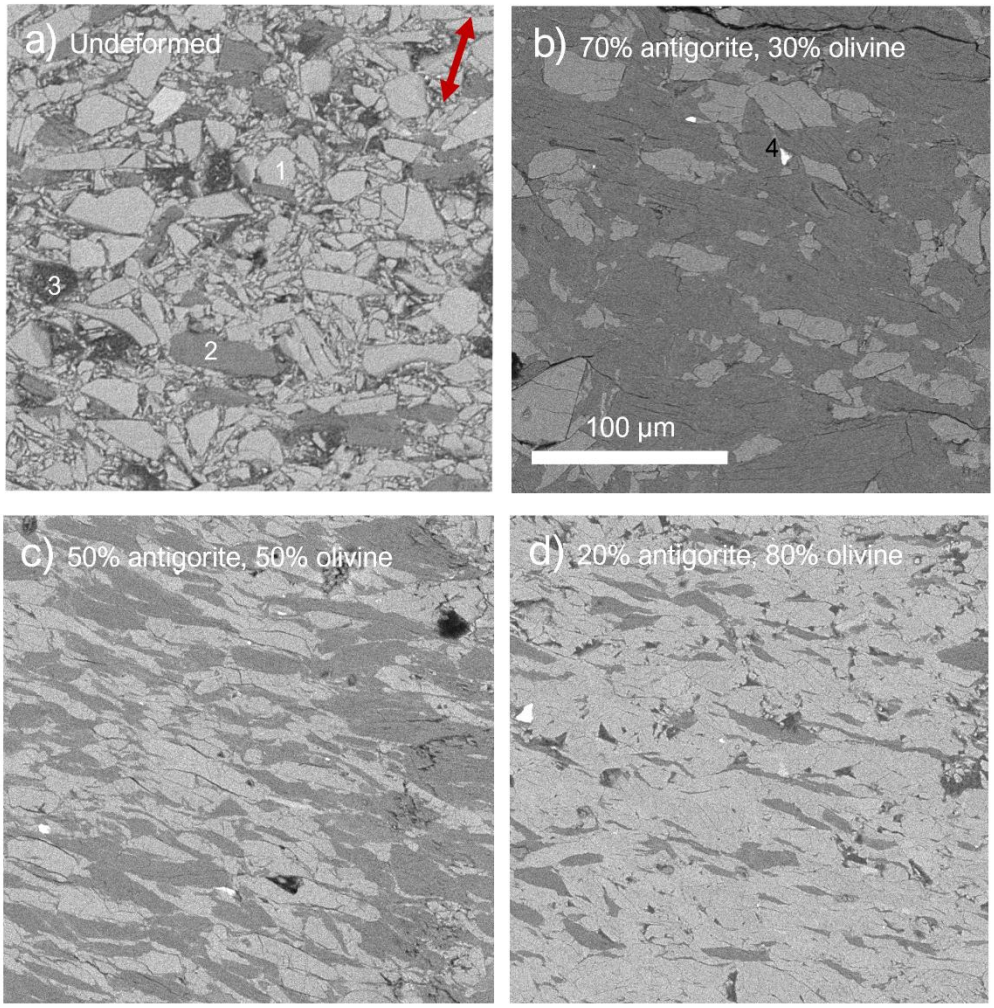

Figure 4. SEM images of undeformed and deformed samples. (a) Image of an undeformed sample with 10 vol.% antigorite and 90 vol.% olivine. Number 1 indicates an olivine grain, number 2 indicates an antigorite grain and number 3 indicates a hole in the sample face from polishing. Red double-sided arrows indicates axial compression direction for all samples. (b) Image of deformed sample D2608. Number 4 indicates a magnetite grain. (c) Image of deformed sample D2646. (d) Image of deformed sample D2703.

state (Castelnau et al., 2008). A set of 3000 crystals with orientations of the initial textures were used, and we defined the reference state with olivine's elastic constants (Zhang and Bass, 2016) at corresponding beginning pressures for each experiment. Deformation evolution was mapped utilizing the evolutions of the measured macroscopic axial strains and hydrostatic stresses. The deformation matrix used in EVPSC can be expressed through the volume change with increasing axial strain for each strain rate step during the simulation (Figure 5).

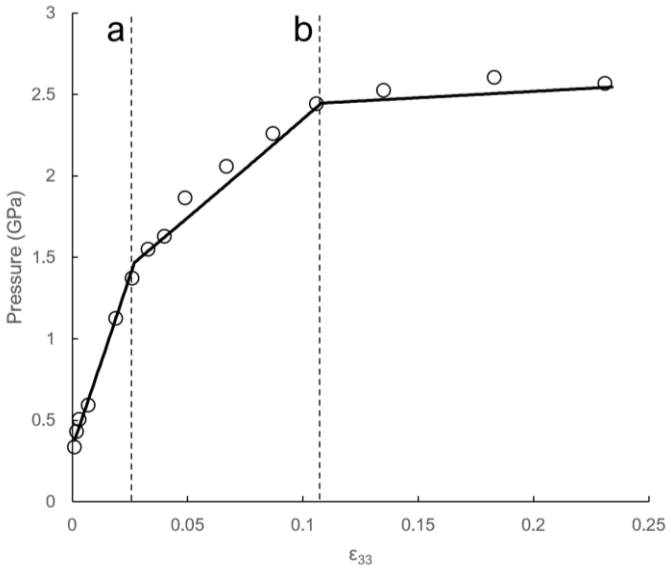

Figure 5. Olivine's pressure versus axial strain ε_{33} for experiment (circles) and EVPSC simulation (solid line) D2609. Dashed line **a** represents the increase in strain rate from $7.42*10^{-6}$ s^{-1} to $2.98*10^{-5}$ s^{-1} and dashed line **b** represents the increase in strain rate from $2.98*10^{-5}$ s^{-1} to $1.18*10^{-4}$ s^{-1}. Volume decrease is equivalent to the hydrostatic stress change seen here, which is used for the EVPSC simulation.

3.4. EBSD Analysis

Thin sections of 5 samples were polished using a 0.3 micron polishing cloth with Al_2O_3 polishing suspensions, then using a vibration polishing machine to remove the mechanical damage. The lattice preferred orientation of olivine and antigorite in four samples was measured on a scanning electron microscope JEOL JSM-6490 equipped with an Oxford Nordlys-S EBSD detector and the Aztec software at State Key Laboratory for Mineral Deposits Research, Nanjing University, China. The thin section was tilted 70° compared to the normal configuration and measured with a working distance of 18–24 mm, an accelerating voltage of 20 kV and a beam current of 4 nA. The EBSD patterns were indexed using the crystal structure of forsterite (Smyth and Hazen, 1973) and antigorite (Capitani and Mellini, 2004). Due to low identification of antigorite by EBSD mapping, we manually scanned the whole section and indexed the mineral phases for individual mineral grains according to the pattern quality and the agreement between detected and simulated Kikuchi bands. The indexed results with the mean angular deviation MAD values of <1 are considered desirable for accurate solutions. Crystallographic orientations of olivine and antigorite were plotted as one point per grain in the lower hemisphere equal-

area projection according to the reference system of deformation experiments (X = stretching lineation; Z = direction of compression) using the Petrophysics program of Mainprice (1990). Unfortunately, for samples D2608, D2609 and D2646, we could not index more than 100 antigorite grains.

Table 2. EVPSC CRSS Parameters[a]

Simulations	(001)[100] & (100)[001]	(010)[100] & (100)[010]	(010)[001]	{011}[100]	{110}[001]	Kink Band Systems[b]
D2608	4.1	4.3	3.4	3.5	3.5	2.3
D2609	1.7	3.2	2.2	2.0	2.0	1.9
D2646	3.1	4.5	3.9	3.5	3.5	2.4
D2647	3.6	4.8	3.5	3.5	3.5	3.1
D2703	5.7	4.7	5.0	4.5	5.0	4.3
D2705	3.7	5.2	6.2	4.5	4.5	4.0
D2708	1.5	6.3	4.1	4.0	4.0	2.5

[a]The hardening parameters, τ_1, θ_0, and θ_1 are equal to 0.01, 0.01, and 0.1 for each simulation.
[b]This group includes {405}<-504>, {405}<50-4> and {120}<-210>

4. RESULTS

Although in theory the pre-sintering of aggregates should only apply hydrostatic stress, minor texture was produced from this procedural step. Olivine developed a (010) or (001) texture and the basal planes of antigorite were compacted perpendicular to the long axis of the cylinder, giving a (100) texture. Lattice strain of the olivine planes are in an order of $Q(101)<Q(002)<Q(130)\cong Q(021)$. The uncertainty for Q(101), Q(130), and Q(021) is ± 0.0005. For Q(002), the error is ± 0.001, due to its much weaker intensity. The uncertainty for antigorite's planes reached ± 0.002, which is likely due to the large peak width caused by its unique texture. Final observed textures of olivine are similar to post-deformation EBSD results, which are discussed in the following sections.

4.1. 70% Antigorite + 30% Olivine

The two samples of 70 vol.% antigorite and 30 vol.% olivine, D2609 and D2608, were compressed up to ~2.5 and ~6.7 GPa, with final estimated differential stresses of 1.7 and 2.3 GPa for olivine, and 1.2 and 1.3 GPa for antigorite, respectively. Q-factors are in an order of $Q(101)<Q(002)<Q(021)<Q(130)$ for both pressures, but the lattice strain of Q(002) is ~0.0005 greater in D2609 (Figure 6). Antigorite maintains a (100) texture which increases in strength with macroscopic strain and indicates glide along its basal plane, while olivine develops a girdle of (010) to (100) texture, with some movement towards the (011) pole (Figure 7). The dominant slip system for both pressures is {011}[100], or pencil glide, and (010)[001], or B-type slip. Both experiments show high activity of the kink systems, which is an observation that applies to all experiments. Figure 4 (b) shows the microstructure of this composition is an interconnected matrix of antigorite with minimal olivine to olivine grain contact.

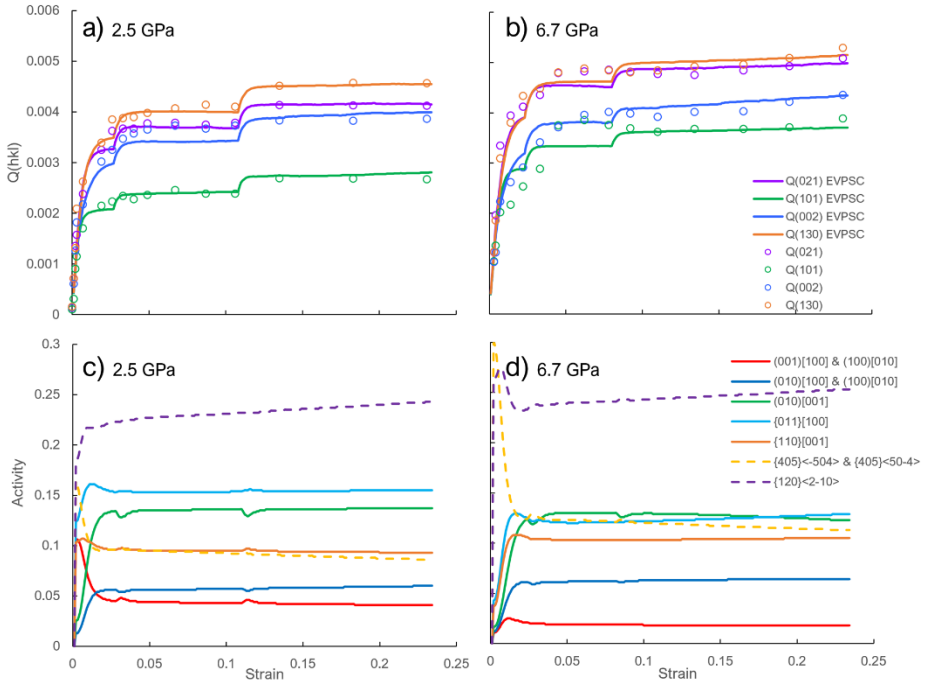

Figure 6. (a) and (b) Experimental and modeled Q(hkl) for olivine in experiments D2609 and D2608, respectively. (c) and (d) slip system activity of olivine. Dashed lines are kink-band systems.

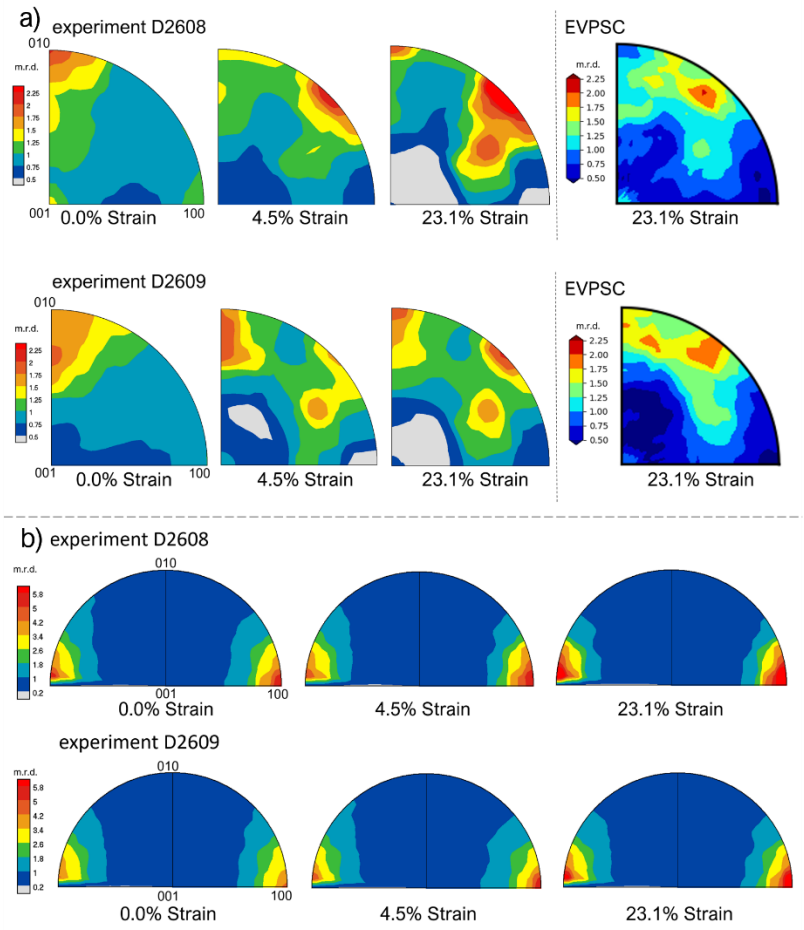

Figure 7. IPFs of experimental and modeled textures of (a) olivine and experimental textures of (b) antigorite. Note the difference in scale bars for the two minerals.

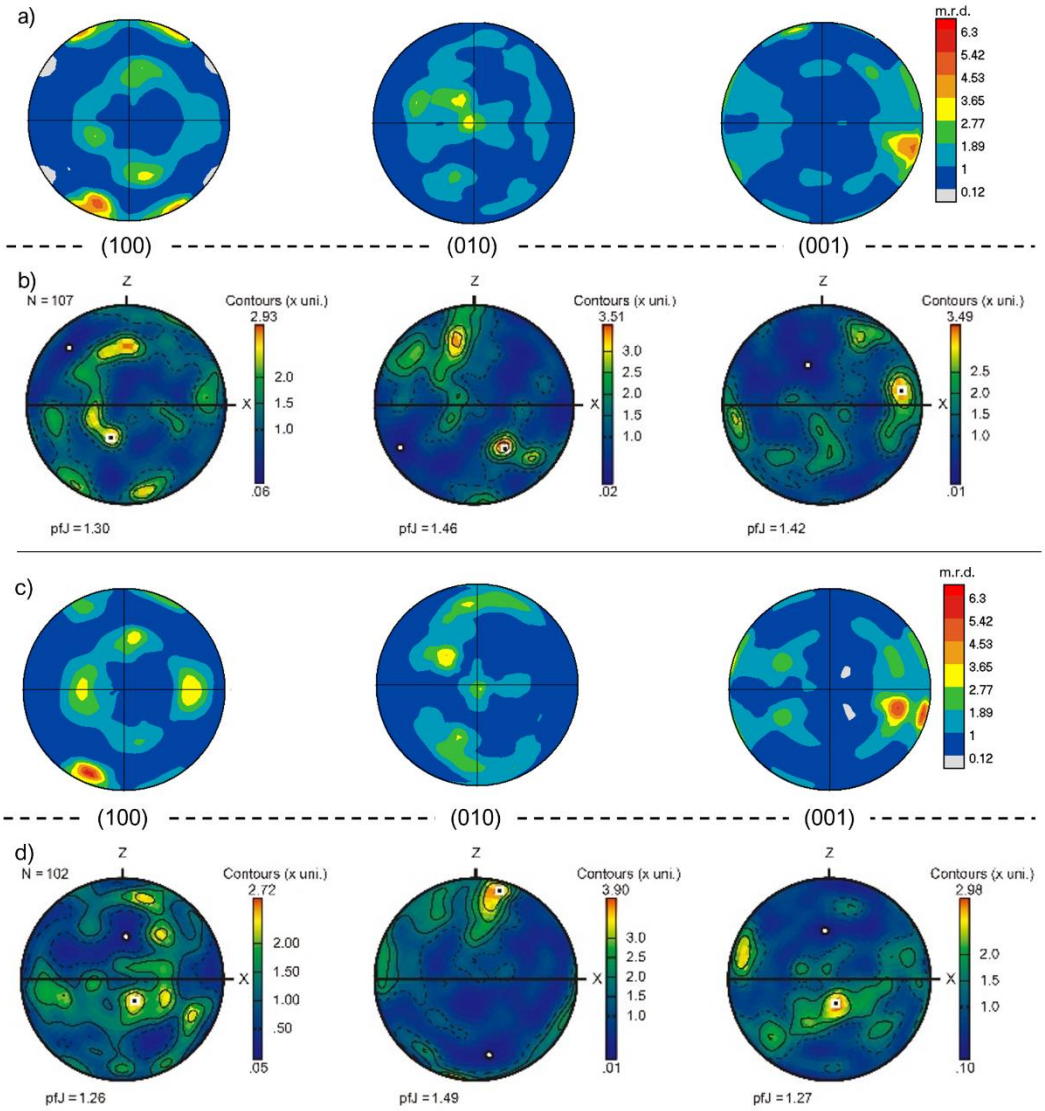

Figure 8. Pole figures for olivine of in-situ final textures (a, c) compared to EBSD results of recovered samples (b, d) for experiments D2608 (a and b) and D2609 (c and d).

Pole figures from EBSD analyses are consistently lower in intensity that the textures collected in situ, which is likely due to the decrease in hydrostatic and differential stress (Figure 8). EBSD pole figures for experiment D2608 are in good agreement with the experimental pole figures, with the (001) pole parallel to lineation and girdles of (100) and (010) poles subparallel to foliation. Pole figures in and ex situ for experiment D2609 are different, with EBSD measurements showing a high density of (010) poles normal to foliation and (001) poles perpendicular to lineation, whereas the in-situ textures show (001)

poles parallel to compression. It is possible textures changed during decompression, which took up to ~10 hr for each sample. An additional factor influencing these differences may be the constrained 2D sampling area of EBSD measurements versus the in-situ x-ray diffraction, which penetrates through the entire width of the sample.

4.2. 50% Antigorite + 50% Olivine

The two samples of 50 vol.% antigorite and 50 vol.% olivine, D2647 and D2646, were compressed up to ~3.7 and ~7.0 GPa, with final estimated differential stresses of 2.6 and 3.0 GPa for olivine, and 1.1 and 1.1 GPa for antigorite, respectively. Q-factors are in order of Q(101)<Q(002)<Q(021)<Q(130) for D2647, but Q(021) and Q(130) are approximately equal for D2646 (Figure 9). Texture evolution for both phases are consistent with observations from D2609 and D2608 (Figure 10), however we see a decrease in texture intensity for both olivine and antigorite. Figure 4 (c) shows the microstructure of this composition includes interconnected layers of both antigorite and olivine.

Similar to results from experiments D2608 and D2609, pole figures from EBSD analyses are lower in intensity than the textures collected in situ (Figure 11). Textures from EBSD analyses show similarities to the in-situ textures, with (001) poles subparallel to lineation direction and both (010) and (100) poles subnormal to foliation direction. Minor differences in textures are likely due to the same reasons stated in the previous section.

4.3. 20% Antigorite + 80% Olivine

The two samples of 20 vol.% antigorite and 80 vol.% olivine, D2703 and D2705, were compressed to ~3.5 and ~6.4 GPa, with final estimated differential stresses of 3.4 and 3.5 GPa for olivine and 1.8 and 1.8 GPa for antigorite, respectively. The beginning texture

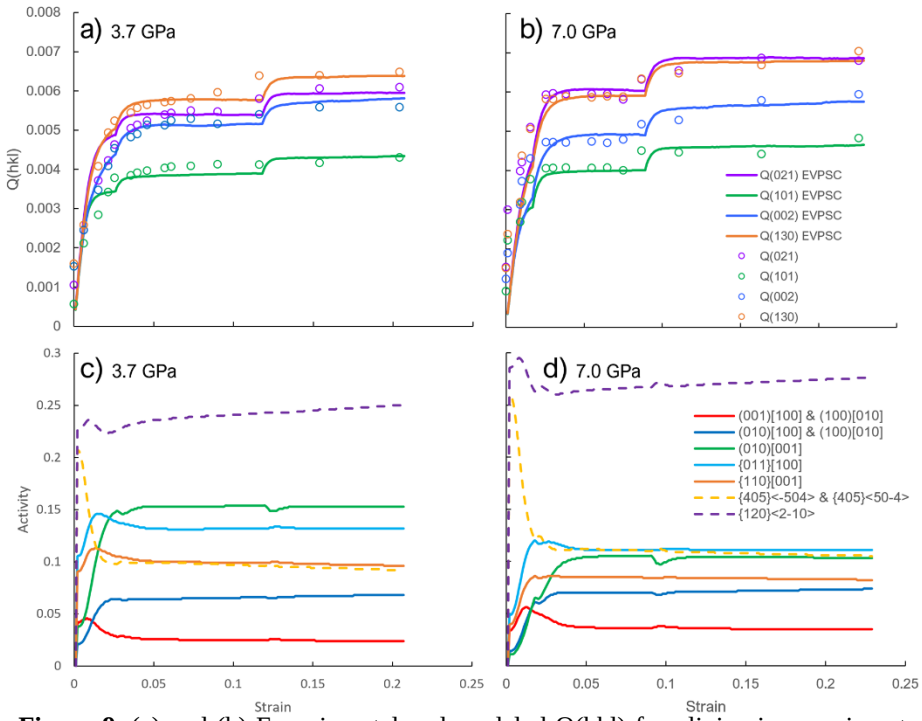

Figure 9. (a) and (b) Experimental and modeled Q(hkl) for olivine in experiments D2647 and D2646, respectively. (c) and (d) slip system activity of olivine. Dashed lines are kink-band systems.

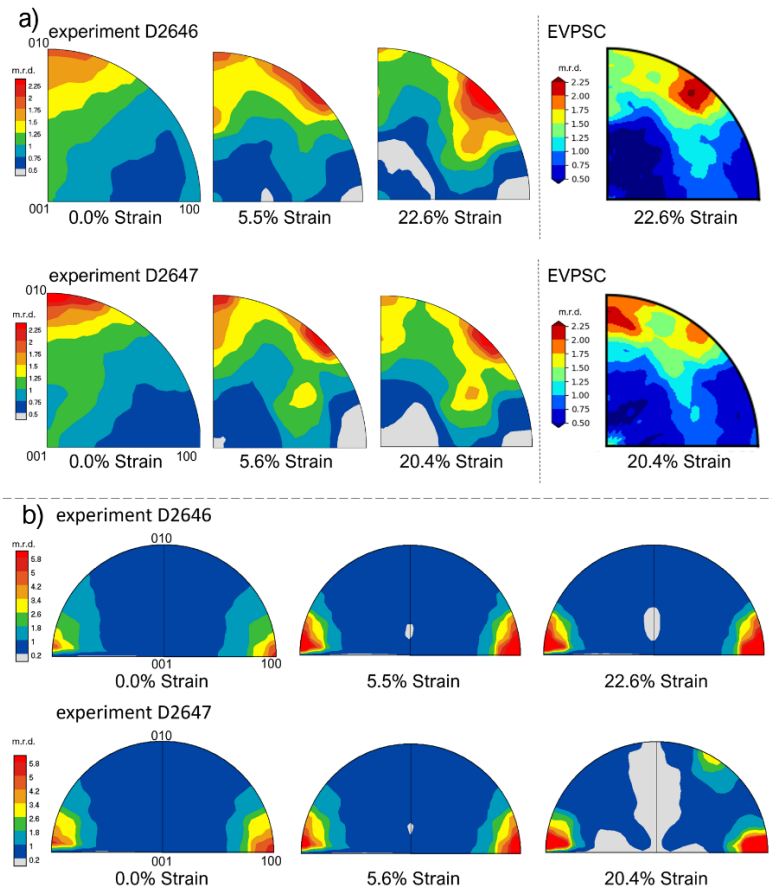

Figure 10. IPFs of experimental and modeled textures of (a) olivine and experimental textures of (b) antigorite. Note the difference in scale bars for the two minerals. For experiment D2647, antigorite shows an artifact of texture near the 110 pole which may be related to a greater amount of (210) planes oriented normal to

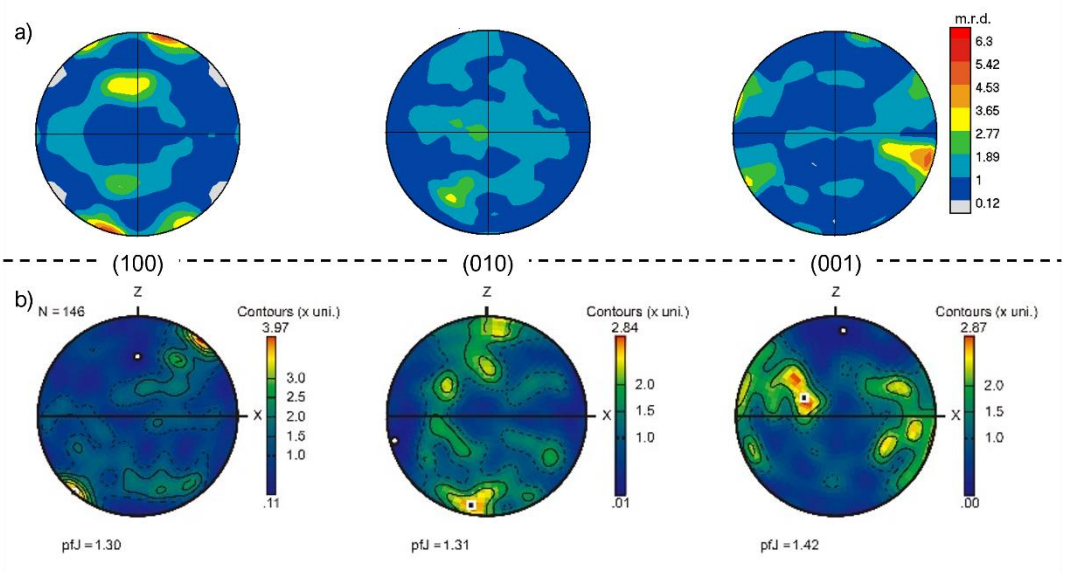

Figure 11. Pole figures for olivine of in-situ final texture (a) compared to EBSD results of recovered sample (b) for experiments D2646.

is slightly different for these experiments, with a higher density of poles near the [001] oriented parallel to compression. Q-factors are in order of Q(101)<Q(002)<Q(130)<Q(021) for both experiments (Figure 12). Again, the basal cleavage of antigorite is oriented perpendicular to the axial compression direction, but the intensity is much lower than the previous four experiments (Figure 13). Olivine textures are consistent in both appearance and intensity as before, but with less pronounced intensity moving towards the (101) pole. Deformation activity again the same as before, but with increased influence from the {110}[001] slip system of olivine, especially in simulation D2705. Figure 4 (d) shows the microstructure of this composition is defined by an olivine framework with pockets of mostly isolated antigorite.

4.4. Experiment D2708

The rotated sample used in experiment D2708 was composed of 50 vol.% antigorite and 50 vol.% olivine. It was compressed to ~7.6 GPa, and final estimated differential

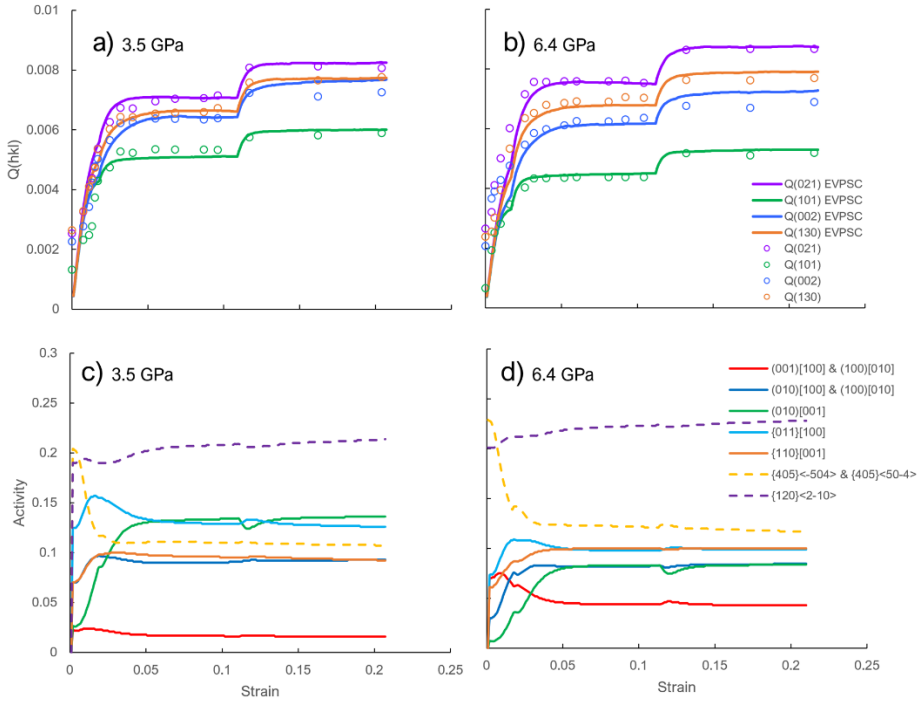

Figure 12. (a) and (b) Experimental and modeled Q(hkl) for olivine in experiments D2703 and D2705, respectively. (c) and (d) slip system activity of olivine. Dashed lines are kink-band systems.

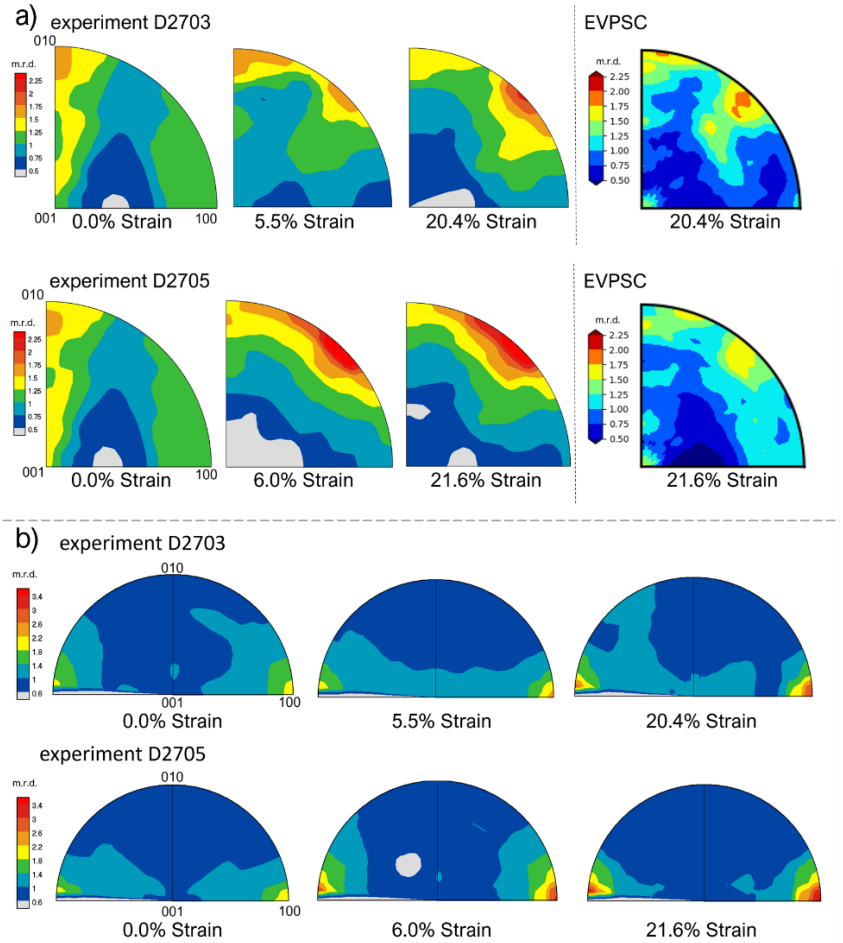

Figure 13. IPFs of experimental and modeled textures of (a) olivine and experimental textures of (b) antigorite. Note the difference in scale bars for the two minerals, here, antigorite intensity is much lower than the previous experiments.

stresses were 2.5 and 2.1 GPa for olivine and antigorite, respectively. The texture prior to deformation appears close to random for both olivine and antigorite. Q-factors are in order of Q(101)<Q(002)<Q(130)<Q(021), but the difference from Q(101) to Q(021), and between each sequential plane, is greater than all the other experimental runs (Figure 14). Antigorite texture begins as a weak girdle from (100) to (001) and develops an obvious (100) texture at the end of deformation (Figure 15). Olivine texture at low strain is near (001) and develops similar texture to the previous experiments at the end of deformation, but with a minor maximum remaining at (001). In this case, the dominant deformation mechanisms are [001](100) and [100](001), or C- and E-type. B-type deformation is still influential, but less so compared to the other experimental runs.

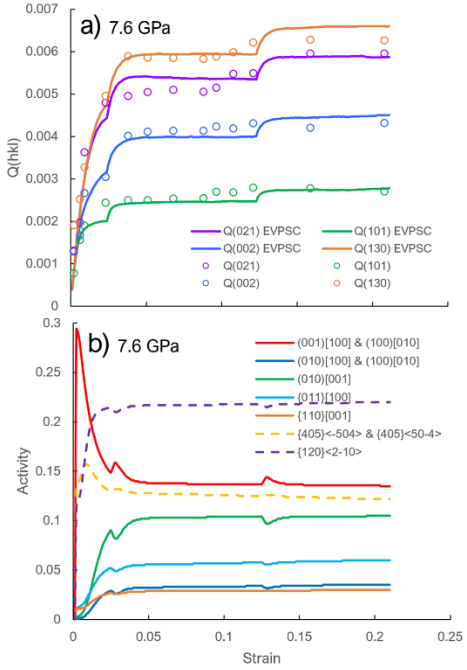

Figure 14. (a) Experimental and modeled Q(hkl) for olivine in experiment D2708. (b) slip system activity of olivine. Dashed lines are kink-band systems.

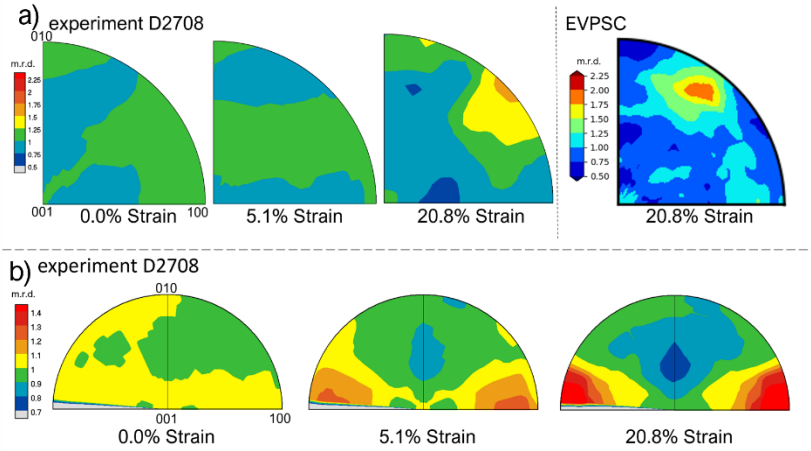

Figure 15. IPFs of experimental and modeled textures of (a) olivine and experimental textures of (b) antigorite. Note the difference in scale bars for the two minerals.

5. DISCUSSION AND IMPLICATIONS

5.1. Stress and Strain

Stresses estimated for olivine from EVPSC and (5) are similar (Figure 16). With increasing olivine content and/or increasing pressure we see an increase in stress, an observation that is useful when interpreting microstructural images (Figure 4). The microstructures of all aggregate compositions show evidence for fairly consistent plastic deformation of antigorite, and variable plastic deformation of olivine. At 30 vol.% of olivine, almost all of the plastic strain appears to be accommodated by antigorite, which has formed an IWL microstructure around the hard clasts of olivine (Figure 4b). Aspect ratio estimations of olivine grains before and after deformation show little to no change. However, olivine still developed texture, so we assume the clasts rotated within the

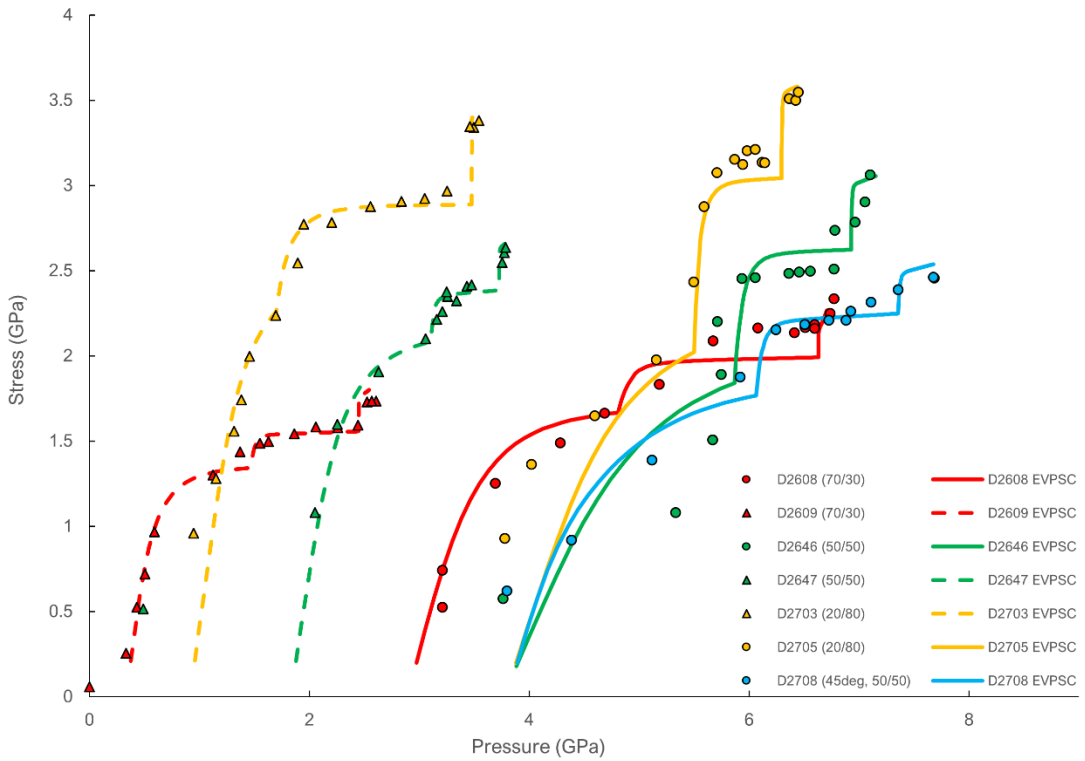

Figure 16. Stress versus Pressure for olivine modeled with EVPSC (solid and dashed lines) and equation 5 (triangles and circles). Error for estimated stress is ±0.25 GPa.

antigorite matrix to their preferred orientations. Volume averaged stress is lower, nearing the single-phase stress of antigorite (Figure 17). Furthermore, the difference in the modeled stress from (5) between phases is at maximum ~1 GPa. Olivine stress appears to be more sensitive to pressure when there is a greater vol.% of antigorite. It is possible that the lower stress conditions when antigorite is abundant are relatively more hydrostatic and makes the pressure effect larger.

At 50 vol.% of olivine the structure is a clast-matrix IWL framework, with both phases interconnected (Figure 4c). Olivine maintains percolation in the compression direction, allowing the volume averaged strength to increase. The antigorite modeled stress from (5) decreased from the previous experiments of 70 vol.% antigorite. When making up 20 vol.% of the aggregate, antigorite grains display a higher degree of strain than experiments with 70 vol.% antigorite. Based on this, at 50 vol.% antigorite grains should have experienced more stress than at 70 vol.% antigorite. The decrease in modeled stress we see for 50 vol.% antigorite is within the calculated error, which is a possible explanation for this anomaly. At 80 vol.% of olivine, the structure appears to have transitioned to LBF regime, with only olivine interconnected, and antigorite existing as weak pockets scattered throughout (Figure 4d). In this case, most of the stress may be supported by olivine. Volume averaged stress is greater than the previous experiments, and the difference in modeled stress between antigorite and olivine is ~2 GPa.

With increasing vol.% of the hard phase we see: (1) an increase in stress difference between the phases and (2) the volume-averaged aggregate stress nears the stress of the harder phase. These observations are similar to the results of the systematic study conducted by Lin et al., (2019), who deformed various phase proportions of two cubic

materials: MgO (hard phase) and NaCl (soft phase). However, when their strong phase vol.% increases from 50 to 80, the stress of the soft phase decreases, likely caused by restricted percolation of the soft phase due to obstruction from the hard phase. In our study, 80 vol.% of olivine saw an increase in stress of antigorite. It is possible that the lower symmetries of antigorite and olivine effect the strain distribution, giving us this difference in stress change from IWL to LBF structure.

It has been suggested that a thin layer of antigorite-rich material exists between the subducting slab and mantle wedge and stretches to greater depths than the serpentinized forearc wedge. One proposed geodynamic effect of this weak interfacial layer is decoupling of the strong mantle wedge from the subducting slab. Wada & Wang's (2009) investigation

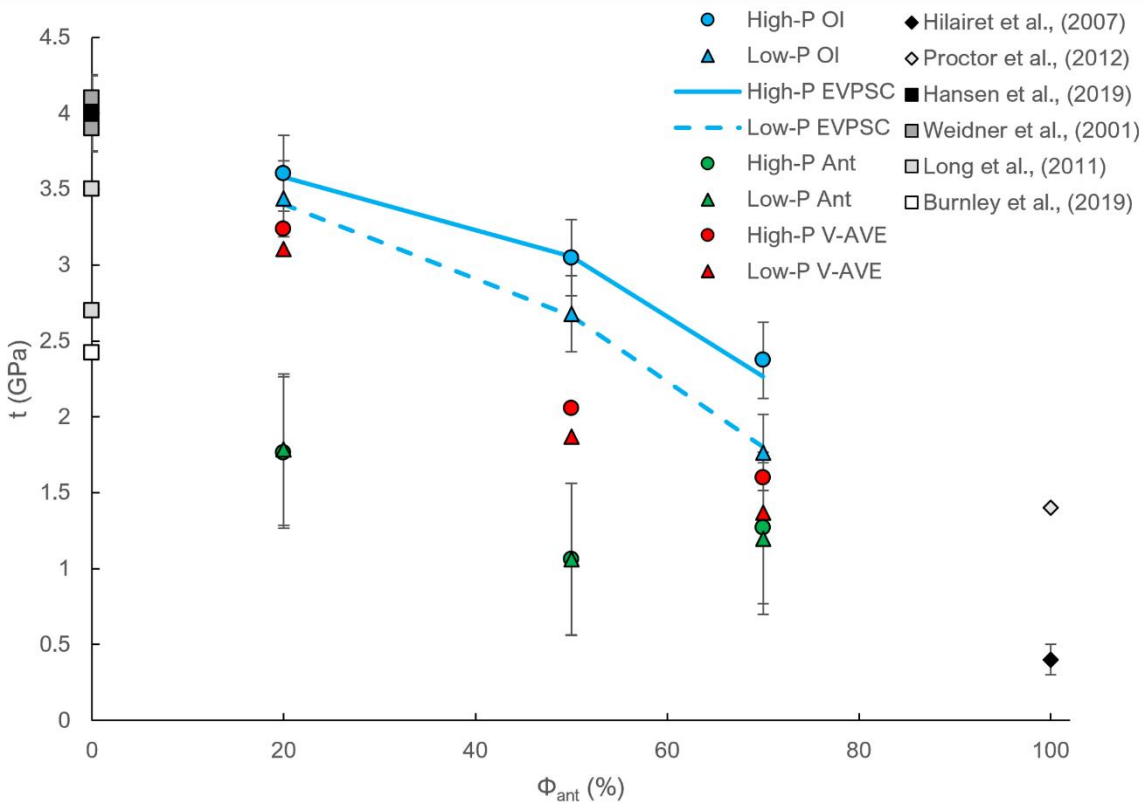

Figure 17. Stress of the individual phases as well as a volumetrically averaged stress. Reference comparisons at similar P, T, grain size, and strain rates are in gray scale with squares for olivine and diamonds for antigorite.

of the maximum depth of decoupling implies the temperature-dependent change in strength of hydrous minerals relative to the strength of mantle minerals may control the extent of decoupling. With reference to Hilairet et al.'s (2007) study, they state an eventual disappearance of the strength contrast between antigorite and olivine with increasing depth and temperature may define the point of transition from decoupling to coupling along the slab. Their model assumes a sharp boundary between the mantle and interface layer defined by distinct changes in temperature related to conductive cooling dominating heat transfer above the interface layer and mantle flow driven convection above the coupled slab. However, a more gradual change of compositions may exist depending on the fluid budget and subduction zone temperature. Seismic observation studies conducted on mantle wedges worldwide show a range in the degree of serpentinization from <10% in cold subduction zones like Tohoku-Hokkaido (Nakajima et al., 2009a, 2009b), 15-25% in intermediate subduction zones like Costa Rica (DeShon and Schwartz, 2004) and Shikoku (Matsubara et al., 2008), and 30% or more in hot subduction zones like Cascadia (Ramachadran and Hyndman, 2012). Determining the precise degree or progression of serpentinization from seismic tomography is difficult due to factors such as poorly defined Mohos between the overriding plate and serpentinized wedge and similar compressional- and shear-wave velocities of many mantle wedge materials (Reynard, 2013). If a gradual compositional change of the serpentinized layer is assumed, the amount of antigorite will decrease with increasing depth and temperature. The experiments conducted here show that with decreasing antigorite proportion, the aggregate increases in strength, and the strength contrast of olivine and antigorite is greater. Temperature was constant in this study so we could not directly investigate the extent of the strength contrast disappearance, but

we can suggest a volumetric decrease of antigorite with depth and temperature may also define the point at which the strength of the interface layer matches that of the overriding mantle, initiating coupling of the slab and mantle. This point of coupling may be where the multiphase structure transitions from an IWL to LBF, or roughly at ~20 vol.% antigorite. Furthermore, the progression of serpentinization may be intertwined with a variation in alignment direction due to convective flow in the hydrated forearc mantle (Nagaya et al., 2016). Along with volume percent of antigorite influencing the shift in microstructure from IWL to LBF, the alignment of antigorite changing from vertical to parallel to the slab will produce different connectivity and seismic anisotropy which may change the conclusions from geophysical observations.

5.2. Texture Evolution and Slip System Activity of Antigorite

In this section of the study, we will refer to antigorite's orientations in the more common second setting, i.e., the basal plane is the (001) plane. CPO of antigorite is very strong, and the increase in intensity with strain provides evidence for progressive compaction of the basal planes. We can only infer the slip systems active in antigorite based on similarities with our textures and previous studies. From EBSD measurements (Figure 18) we see a high density of (001) poles parallel to compression, and a girdle of (010) and (001) poles parallel to lineation prior to deformation. In experiment D2708, we see migration of (010) and (100) poles to the more common orientation of (001). These observations lead us to assume there is activation of both common slip systems observed in antigorite; the (001)[100] (reported by Bezacier et al., 2010, Katayama et al., 2009, Van de Moortele et al, 2010, Padron-Navarta et al., 2012, Morales et al., 2018) and [010](001) (reported by Jung, 2011, Brownlee et al., 2013, Nishii et al., 2011, Soda and Wenk, 2013,

Hirauchi et al., 2010) systems. Previous studies have proposed dominant activation of one or the other slip system, but many also declare equal activation, glide on [hk0](001), or deformation primarily through sliding of shear cracks or bands (e.g. Padron-Navarta et al., 2012, Auzende et al, 2015, Hansen et al., 2020). As vol.% of antigorite decreases, the texture evolves the same for each experiment (disregarding early strain in experiment D2708) with the singular difference of decreasing intensity. This fact coupled with CPO similarities from other studies can allow us to conclude that antigorite deforms like it would as a single phase when mixed with olivine regardless of its volume proportion.

5.3. Texture Evolution and Slip System Activity of Olivine

For all deformation sequences, we see high activity of the unidirectional kink band systems. According to the von Mises criterion, five independent slip systems are required for arbitrary plastic deformation of an olivine crystal (von Mises, 1913). The seven commonly observed slip systems we used in the modeling only included two independent

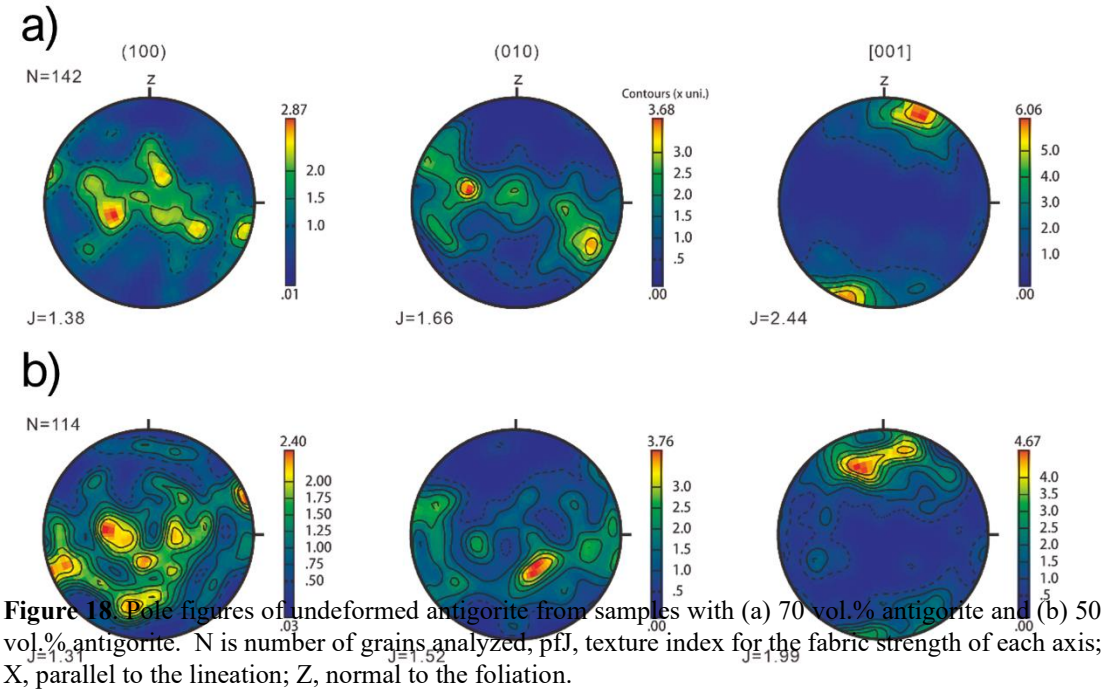

Figure 18. Pole figures of undeformed antigorite from samples with (a) 70 vol.% antigorite and (b) 50 vol.% antigorite. N is number of grains analyzed, pfJ, texture index for the fabric strength of each axis; X, parallel to the lineation; Z, normal to the foliation.

slip systems ([100]{011} and [001]{110}), so the addition of kink bands with low CRSS values allowed axial deformation along all lattice directions. All kink systems are very active, especially at early strain, implying they greatly influence the transient deformation. The $<2\bar{1}0>\{120\}$ system is especially active, compensating for ~20-30% of total activity. Burnley et al., (2015) suggests this system specifically weakens grains with [100] near the compression direction but a spread of orientations may be affected by any given kink band. It is possible that this specific system affects grains with [010] near the compression direction as well, which is the beginning CPO of most of our samples and is therefore the most important system for weaking the majority of olivine grains. Additionally, the conditions here are assumed to be hydrated due to the addition of antigorite, which contains ~13 weight percent water (Ulmer and Trommsdorf, 1997). This reduces the Peierls stress and subsequently increases kink concentration and rate of deformation due to that kink system (Katayama and Karato, 2008, Karato et al., 2008). There is a systematic increase in kink system activity with increasing P, perhaps due to decreased ability to slide at greater P.

Activity of the seven commonly observed slip systems is fairly consistent for all experiments except D2708. Previous studies have shown that the main slip systems of olivine under low-T, high-stress, similar strain rates, and hydrated conditions are B-type and pencil glide (Jung and Karato, 2001, Wenk et al., 2004, Karato et al., 2008, Bernard et al., 2019), which are indeed the two most active non-kink systems here. Experiments D2703 and D2705 experience a change in lattice reflections (130) and (021), a contradicting observation to Nishihara et al. (2010), who reported the opposite change with increasing pressure. There are two observations that should be brought up regarding the

experiments D2703 and D2705; (1) the beginning girdle of texture from (001) to (010) differs from the strong (010) texture in the previous experiments and (2) the slip system [001]{110} is more active, especially in D2705. These differences may account for the cross over in Q(hkl) values, although the quantitative change is within error for those lattice planes. It is likely that the different initial textures prevented production of the pronounced girdle stretching almost to the (101) pole observed in the previous four experiments.

Experiment D2708 has an obvious change in slip system activity, implying that the original orientation of olivine and antigorite likely has an effect on the deformation behavior of this two-phase mixture, especially the transient deformation. It should be noted that this experiment reached the highest pressure at the final strain, however, it is still in the stability field of both phases. This olivine appears to be mostly experiencing C-type and E-type slip, especially during initial strain increase, which is likely connected to the higher density of (100) poles parallel to compression direction. These slip systems are commonly observed in lower-stress regimes than B-type slip and have been suggested to be the dominant slip systems in the ambient mantle and dry volcanic arc to back arc mantle wedge (Bernard et al., 2019, Karato et al., 2008). However, this sample was deformed at hydrated, forearc mantle wedge conditions. This, along with the other experimental runs (in particular D2646 and D2647), demonstrates the importance of pre-existing textures of the aggregate to the deformation behaviors of olivine.

6. CONCLUSIONS

High-P, -T deformation experiments performed on aggregates consisting of varying volume proportions of antigorite and olivine coupled with EVPSC modeling, EBSD, and image analysis allowed us to make the following conclusions:

(1) Through EVPSC, were able to reproduce good fits to both texture and lattice strains for olivine using commonly observed slip systems and kink bands.

(2) Volume average stress increases with increasing olivine content, consistent with Handy's (1990, 1994) predictions based on a transition from IWL to LBF microstructures. This may have implications for determining the point of minimum strength contrast between the serpentinized interface layer and mantle wedge responsible for coupling of the mantle and subducting slab.

(3) When mixed with any volume proportion of olivine and a strong alignment of (001) planes parallel to foliation, antigorite deforms like it would as a single phase, with inferred dislocation gliding of the slip systems [100](001) and [010](001), which is consistent with microstructural analyses of exhumed serpentinized peridotites.

(4) When mixed with antigorite, olivine deforms dominantly with unidirectional kink systems and the [100]{011} and [001](010) slip systems, which are common slip systems for high-stress, low-T and hydrated mantle conditions.

(5) Pre-existing textures change deformation mechanisms for olivine. It is possible that texture formed under hydrostatic stress may differ when this aggregate has an LBF or a IWL structure. This conclusion may not apply to formation textures under high differential stress settings like subduction zones

but is important to consider when conducting laboratory scale multiphase experiments.

References

Auzende, A. L., Escartin, J., Walte, N. P., Guillot, S., Hirth, G., & Frost, D. J. (2015). Deformation mechanisms of antigorite serpentinite at subduction zone conditions determined from experimentally and naturally deformed rocks. Earth and Planetary Science Letters, 411, 229-240. https://doi.org/10.1016/j.epsl.2014.11.053

Bernard, R. E., Behr, W. M., Becker, T. W., & Young, D. J. (2019). Relationships between olivine CPO and deformation parameters in naturally deformed rocks and implications for mantle seismic anisotropy. Geochemistry, Geophysics, Geosystems, 20(7), 3469-3494.

Bezacier, L., Reynard, B., Bass, J. D., Sanchez-Valle, C., & Van de Moortèle, B. (2010). Elasticity of antigorite, seismic detection of serpentinites, and anisotropy in subduction zones. Earth and Planetary Science Letters, 289(1-2), 198-208.

Bezacier, L., B. Reynard, H. Cardon, G. Montagnac, J.D. Bass, (2013) High-pressure elasticity of serpentine and seismic properties of the hydrated mantle wedge. J. Geophys. Res.: Solid Earth, 118 (2013), 527-535, 10.1002/jgrb.50076

Birch, F., (1947), Finite elastic strain of cubic crystals. Phy. Rev. 71(11), 809

Brownlee, S. J., Hacker, B. R., Harlow, G. E., & Seward, G. (2013). Seismic signatures of a hydrated mantle wedge from antigorite crystal-preferred orientation (CPO). Earth and Planetary Science Letters, 375, 395-407.

Burnley, P., (2015). Elastic plastic self-consistent (EPSC) modeling of plastic deformation in fayalite olivine. American Mineralogist Special Collection: Olivine, 100, 1424-1433. http://dx.doi.org/10.2138/am-2015-5234CCBYNCND

Burnley, P., Kaboli, S., (2019). Elastic plastic self-consistent (EPSC) modeling of San Carlos olivine deformed in a D-DIA apparatus. American Mineralogist, 104, 276-281. https://doi.ord/10.2138/am-2019-6666

Burnley, P.C., and Zhang, D. (2008) Interpreting in situ X-ray diffraction data from high pressure deformation experiments using elastic-plastic self-consistent models: an example using quartz. Journal of Physics: Condensed Matter, 20(28), 10. https://doi.org/10.1088/0953-8984/20/28/285201

Capitani G, Mellini M. (2004). The modulated crystal structure of antigorite: The m = 17 polysome. American Mineralogist, 89, 147-158.

Castelnau, O., Blackman, D. K., Lebensohn, R., Ponte Castaneda, P., (2008). Micromechanical modeling for the Viscoplastic behavior of olivine. . J. Geophys. Res.: Solid Earth, 113 (B9), https://doi.org/10.1029/2007JB005444

Chandler, B., Bernier, J., Diamond, M., Kunz, M., Wenk, H-R., (2021), Exploring microstructures in lower mantle mineral assemblages with synchrotron x-rays. Science Advances, 7 (1). https://doi.org/10.1126/sciadv.abd3614

DeShon, H.R., Schwartz, S.Y., (2004). Evidence for serpentinization of the forearc mantle wedge along the Nicoya Peninsula, Costa Rica. Geophysical Research Letters 31.

Girard, J., Amulele, G., Farla, R., Mohiuddin, A., Karato, S.-I., (2016). Shear deformation of bridgmanite and magnesiowustite aggregates at lower mantle conditions, Science, 351 (6269), 144-147. https://doi.org/10.1126/science.aad3113

Handy, M.R, (1994). Flow laws for rocks containing two non-linear viscous phases: A phenomenological approach. Journal of Structural Geology, 16, 287-301.

Handy, M.R. (1990). The solid-state flow of polymineralic rocks. Journal of Geophysical Research: Solid Earth, 95, 8647-8661.

Hilairet, N., Reynard, B., Wang, Y., Daniel, I., Merkel, S., Nishiyama, N., & Petitgirard, S. (2007). High-Pressure Creep of Serpentine, Interseismic Deformation, and Initiation of Subduction. Science, 318(5858), 1910–1913. https://doi.org/10.1126/science.1148494

Hilairet, N., Wang, Y., Sanehira, T., Merkel, S., Mei, S. (2012). Deformation of olivine under mantle conditions: An in situ high-pressure, high-temperature study using monochromatic synchrotron radiation. Journal of Geophysical Research, 117, B01203, https://doi.org/10.1029/2011JB008498

Hirauchi, K. I., Michibayashi, K., Ueda, H., & Katayama, I. (2010). Spatial variations in antigorite fabric across a serpentinite subduction channel: Insights from the Ohmachi Seamount, Izu-Bonin frontal arc. Earth and Planetary Science Letters, 299(1-2), 196-206.

Horn, C., Bouilhol, P., & Skemer, P. (2020). Serpentinization, deformation, and seismic anisotropy in the subduction mantle wedge. Geochemistry, Geophysics, Geosystems, 21, e2020GC008950. https://doi.org/10.1029/2020GC008950

Jung, H. (2011). Seismic anisotropy produced by serpentine in mantle wedge. Earth and Planetary Science Letters, 307(3-4), 535-543.

Jung, H., & Karato, S. I. (2001). Water-induced fabric transitions in olivine. Science, 293(5534), 1460-1463.

Karato, S. I., Jung, H., Katayama, I., & Skemer, P. (2008). Geodynamic significance of seismic anisotropy of the upper mantle: New insights from laboratory studies. Annu. Rev. Earth Planet. Sci., 36, 59-95.

Kasemer, M., Eloisa Zepeda-Alarcon, Robert Carson, Paul Dawson, Hans-Rudolf Wenk, (2020), Deformation heterogeneity and intragrain lattice misorientation in high strength contrast, dual-phase bridgmanite/periclase, Acta Materialia, 189, 284-298, ISSN 1359-6454, https://doi.org/10.1016/j.actamat.2020.02.061

Katayama, I., Haemyeong Jung, Shun-ichiro Karato (2004). New type of olivine fabric from deformation experiments at modest water content and low stress. Geology, 32 (12): 1045–1048. https://doi.org/10.1130/G20805.1

Katayama, I., Hirauchi, K. I., Michibayashi, K., & Ando, J. I. (2009). Trench-parallel anisotropy produced by serpentine deformation in the hydrated mantle wedge. Nature, 461(7267), 1114–1117. https://doi.org/10.1038/nature08513

Katayama, I., Shun-ichiro Karato, (2008) Low-temperature, high-stress deformation of olivine under water-saturated conditions, Physics of the Earth and Planetary Interiors, 168 (3–4), 125-133, ISSN 0031-9201, https://doi.org/10.1016/j.pepi.2008.05.019

Kayima, S.I., Kobayashi, Y., (2000). Seismological evidence for the existence of serpentinized wedge mantle. Geophysical Research Letters. 27 (6), 819-822. https://doi.org/10.1029/1999GL011080

Kenyon, L., Wada, I., (2022). Mantle Wedge Seismic Anisotropy and Shear Wave Splitting: Effects of Oblique Subduction. Journal of Geophysical Research: Solid Earth, 127, 4, https://doi.org/10.1029/2021JB022752

Lebensohn, R., & Tomé, C. N. (1994). A self-consistent viscoplastic model: prediction of rolling textures of anisotropic polycrystals. Materials Science and Engineering: A, 175(1-2), 71-82.

Li, L., Donald Weidner, Paul Raterron, Jiuhua Chen, Michael Vaughan, 2004, Stress measurements of deforming olivine at high pressure, Physics of the Earth and Planetary Interiors,143–144, 357-367, ISSN 0031-9201, https://doi.org/10.1016/j.pepi.2003.09.022

Long, M. D., & van der Hilst, R. D. (2006). Shear wave splitting from local events beneath the Ryukyu arc: Trench-parallel anisotropy in the mantle wedge. Physics of the Earth and Planetary Interiors, 155(3–4), 300–312. https://doi.org/10.1016/j.pepi.2006.01.003

Long, M. D., & Wirth, E. A. (2013). Mantle flow in subduction systems: The mantle wedge flow field and implications for wedge processes. Journal of Geophysical Research: Solid Earth, 118(2), 583–606. https://doi.org/10.1002/jgrb.50063

Lutterotti, L., Matthies, S., Wenk, H. R., Schultz, A. S., & Richardson, J. W. (1997). Combined texture and structure analysis of deformed limestone from time-of-flight neutron diffraction spectra. Journal of Applied Physics, 81(2), 594–600. https://doi.org/10.1063/1.364220

Mainprice, D. (1990). A FORTRAN program to calculate seismic anisotropy from the lattice preferred orientation of minerals. Computers & Geosciences **16**, 385–393.

Matsubara, M., Obara, K., Kasahara, K., (2008). Three-dimensional P- and S-wave velocity structures beneath the Japan Islands obtained by high-density seismic stations by seismic tomography. Tectonophysics 454, 86–103

Matthies, S. & Wenk, H.-R. (2009). Transformations for monoclinic crystal symmetry in texture analysis. J. Appl. Cryst. 42, 564-571. https://doi.org/10.1107/S0021889809018172

Matthies, S., & Vinel, G. W. (1982). On the reproduction of the orientation distribution function of texturized samples from reduced pole figures using the conception of a conditional ghost correction. physica status solidi (b), 112(2), K111-K114.

Miyagi, L., Wenk, H.R. (2016). Texture development and slip systems in bridgmanite and bridgmanite+ ferropericlase aggregate. Physics and Chemistry of Minerals, 43, 597-613. https://doi.org/10.1007/s00269-016-0820-y

Morales, L., David Mainprice, Hartmut Kern, Olivine-antigorite orientation relationships: Microstructures, phase boundary misorientations and the effect of cracks in the seismic properties of serpentinites, Tectonophysics, 724–725, 2018, 93-115,ISSN 0040-1951, https://doi.org/10.1016/j.tecto.2017.12.009

Nagaya, T., Walker, A. M., Wookey, J., Wallis, S. R., Ishii, K., & Kendall, J. (2016). Seismic evidence for flow in the hydrated mantle wedge of the Ryukyu subduction zone. Scientific reports, 6(1), 1-13. DOI: 10.1038/srep29981

Nakajima, J., Tsuji, Y., Hasegawa, A., (2009a). Seismic evidence for thermally-controlled dehydration reaction in subducting oceanic crust. Geophysical Research Letters 36.

Nakajima, J., Tsuji, Y., Hasegawa, A., Kita, S., Okada, T., Matsuzawa, T., (2009b). Tomographic imaging of hydrated crust and mantle in the subducting Pacific slab be- neath Hokkaido, Japan: evidence for dehydration embrittlement as a cause of intraslab earthquakes. Gondwana Research 16, 470–481.

Nishihara, Y., K. Funakoshi, Y. Higo, N. Tsujino, T. Kawazoe, T. Kubo, A. Shimojuku, H. Terasaki, and N. Nishiyama (2010), Stress relaxation experiments of olivine under conditions of subducted slab in Earth's deep upper mantle, Phys. Earth Planet. Inter., 183(1–2), 164–174, doi:10.1016/ j.pepi.2010.07.006.

Nishii, A., S.R. Wallis, T. Mizukami, K. Michibayashi, (2011), Subduction related antigorite CPO patterns from forearc mantle in the Sanbagawa belt, southwest Japan, Journal of Structural Geology, 33, Issue 10, 1436-1445, ISSN 0191-8141, https://doi.org/10.1016/j.jsg.2011.08.006

Padrón-Navarta, J. A., Tommasi, A., Garrido, C. J., & Sánchez-Vizcaíno, V. L. (2012). Plastic deformation and development of antigorite crystal preferred orientation in high-pressure serpentinites. Earth and Planetary Science Letters, 349, 75-86.

Ramachandran, K., Hyndman, R.D., 2012. The fate of fluids released from subducting slab in Northern Cascadia. Solid Earth 3, 121–129.

Reynard, B. (2013). Serpentine in active subduction zones. Lithos, 178, 171-185. https://doi.org/10.1016/j.lithos.2012.10.012

Singh, A. K., C. Balasingh, H. K. Mao, R. J. Hemley, and J. F. Shu (1998), Analysis of lattice strains measured under nonhydrostatic pressure, J. Appl. Phys., 83(12), 7567–7575, doi:10.1063/1.367872

Smyth J. R, Hazen R M. (1973). The crystal structures of forsterite and hortonolite at several temperatures up to 900 ºC. American Mineralogist 58, 588-593

Soda, Y., & Wenk, H. R. (2014). Antigorite crystallographic preferred orientations in serpentinites from Japan. Tectonophysics, 615–616, 199–212. https://doi.org/10.1016/j.tecto.2013.12.016

Tome, C., Canova, G. R., Kocks, U. F., Christodoulou, N., & Jonas, J. J. (1984). The relation between macroscopic and microscopic strain hardening in FCC polycrystals. Acta metallurgica, 32(10), 1637-1653.

Turner, P. A., & Tomé, C. N. (1994). A study of residual stresses in Zircaloy-2 with rod texture. Acta metallurgica et Materialia, 42(12), 4143-4153.

Ulmer, P., & Trommsdorff, V. (1995). Serpentine Stability to Mantle Depths and Subduction-Related Magmatism. In New Series (Vol. 268, Issue 5212).

van de Moortèle, B., Bezacier, L., Trullenque, G., & Reynard, B. (2010). Electron back-scattering diffraction (EBSD) measurements of antigorite lattice-preferred orientations (LPO). Journal of microscopy, 239(3), 245-248.

van Keken, P. E. (2003). The structure and dynamics of the mantle wedge. Earth and Planetary Science Letters, 215(3–4), 323–338. https://doi.org/10.1016/S0012-821X(03)00460-6

von Mises, R. (1913). Mechanik der festen Korper im plastisch deformablen Zustand, Nachrichten von der Koniglichen Gessellschaft der Wissenschaften zu Goettingen, Mathematisch-physikalische Klasse, 582-592.

Wada, I., & Wang, K. (2009). Common depth of slab-mantle decoupling: Reconciling diversity and uniformity of subduction zones. Geochemistry, Geophysics, Geosystems, 10(10). https://doi.org/10.1029/2009GC002570

Wada, I., Wang, K., He, J., & Hyndman, R. D. (2008). Weakening of the subduction interface and its effects on surface heat flow, slab dehydration, and mantle wedge serpentinization. Journal of Geophysical Research: Solid Earth, 113(4), 1–15. https://doi.org/ 10.1029/2007JB005190

Wang, H., P.D. Wu, C.N. Tomé, Y. Huang, (2010) A finite strain elastic–viscoplastic self-consistent model for polycrystalline materials, Journal of the Mechanics and Physics of Solids, 58 (4),b594-612, https://doi.org/10.1016/j.jmps.2010.01.004

Wenk, H. R., Matthies, S., Donovan, J., & Chateigner, D. (1998). BEARTEX: a Windows-based program system for quantitative texture analysis. Journal of Applied Crystallography, 31(2), 262-269.

Wenk, H.-R., Lonardelli, I., Pehl, J., Devine, J., Prakapenka, V., Shen, G., Mao, H. -K., (2004). In situ observation of texture development in olivine, ringwoodite, magneiowustite and silicate perovskite at high pressure. Earth and Planetary Science Letters, 226, 507-529. https://doi.org/10.1016/j.epsl.2004.07.003

Wiens, D., Conder, J., Faul, U., (2008). The Seismic Structure and Dynamics of the Mantle Wedge. Annual Review of Earth and Planetary Sciences, 36, 421-455. https://doi.org/10.1146/annurev.earth.22.092203.122633

Zhang, J. S., & Bass, J. D. (2016). Sound velocities of olivine at high pressures and temperatures and the composition of Earth's upper mantle. Geophysical Research Letters, 43(18), 9611-9618. https://doi.org/10.1002/2016GL069949

Zhang, S., Karato, Si. (1995). Lattice preferred orientation of olivine aggregates deformedin simple shear. Nature 375, 774–777. https://doi.org/10.1038/375774a0